

V₂C MXene-modified g-C₃N₄ for enhanced visible-light photocatalytic activity

Ruizheng Xu, Guiyu Wei, Zhemin Xie, Sijie Diao, Jianfeng Wen, Tao Tang,

Li Jiang, Ming Li ^{a,*}, Guanghui Hu ^{a,*}

College of Science & Key Laboratory of Low-dimensional Structural Physics and Application,
Education Department of Guangxi Zhuang Autonomous Region, Guilin University of Technology,
Guilin 541004, China

*E-mail addresses: 2006017@glut.edu.cn (M. Li), guanghui@glut.edu.cn (G. Hu).

ABSTRACT

Increasing the efficiency of charge transfer and separation efficiency of photogenerated carriers are still the main challenges in the field of semiconductor-based photocatalysts. Herein, we synthesized g-C₃N₄@V₂C MXene photocatalyst by modifying g-C₃N₄ using V₂C MXene. The prepared photocatalyst exhibited outstanding photocatalytic performance under visible light. The degradation efficiency of methyl orange by g-C₃N₄@V₂C MXene photocatalyst was as high as 94.5%, which is 1.56 times higher than that by g-C₃N₄. This was attributed to the V₂C MXene inhibiting the rapid recombination of photogenerated carriers and facilitating rapid transfer of photogenerated electrons (e⁻) from g-C₃N₄ to MXene. Moreover, g-C₃N₄@V₂C MXene photocatalyst showed good cycling stability. The photocatalytic performance was higher than 85% after three cycles. Experiments to capture free radicals revealed that superoxide radicals ($\cdot\text{O}_2^-$) are the main contributors to the photocatalytic activity. Thus, the proposed g-C₃N₄@V₂C MXene photocatalyst is a promising visible-light catalyst.

Keywords: g-C₃N₄; V₂C MXene; Photocatalyst; Cocatalyst; Charge transfer; Separation efficiency

1 Introduction

Various synthetic dyes are directly released into water bodies, causing severe water pollution. Anionic azo dyes are the most commonly used synthetic dyes. Methyl orange (MO) is a common anionic azo dye that is very poisonous and carcinogenic to humans. Semiconductor-based photocatalysts are one of the most effective means of harvesting solar energy for tackling the energy and environmental crisis and are highly promising for reducing such water pollution issues [1]. Several semiconductor photocatalysts, including CdS, TiO₂, Bi₂WO₆, BiVO₄, and g-C₃N₄, have been studied over the last decade [2-5]. Among them, g-C₃N₄ is frequently utilized for pollutant degradation because of its superior performance, nontoxicity, nonmetallic composition, and distinctive electronic band structure. However, its photocatalytic activity is constrained by low light absorption, slow charge transfer, and high carrier recombination rate. Therefore, Zhuang et al. have focused on improving the separation efficiency and charge transfer rate of electron–hole pairs in g-C₃N₄ [6].

Modification of g-C₃N₄ using cocatalysts is known to improve the above properties of g-C₃N₄. Cocatalysts usually include various materials, such as nanoparticles, carbon nanotubes, graphene quantum dots, MXene, 2D MoS₂/graphene (MG), LaFeO₃ and LaNiO₃ [7-14]. For instance, the reaction rate constant *k* value of 2D CN/MG ternary photocatalyst prepared by in situ adsorption method was 4.8 times higher than that of pure g-C₃N₄ [12]. Zhang et al. synthesized Ag/g-C₃N₄/LaFeO₃ Z-scheme heterojunction photocatalysts with degradation rates of 98.97% and 94.94% for methylene blue and tetracycline hydrochloride [13]. In addition, Bao et al. fabricated highly efficient LaNiO₃/g-C₃N₄/MoS₂ photocatalyst, which effectively promoted water decomposition and pollutant degradation [14]. Among them, MXene, which can be used as cocatalyst in place of precious metals, have been the focus of extensive research in the last decade in the fields of environmental pollution and catalysis. Ti₃C₂, the first reported MXene, is widely employed in photocatalysis owing to its unique accordion-like nanosheet structure, excellent electrical conductivity, high carrier mobility, and various active groups at the surface terminus. Notably, V₂C MXene has a morphology similar to that of Ti₃C₂ MXene but possesses a greater specific surface area and more active centers, thus making it a promising cocatalyst for pollutant degradation [15]. Zhou et al. have recently synthesized a three-dimensional porous ZnO/V₂C MXene using V₂C MXene as a cocatalyst [16]. V₂C MXene promoted carrier separation and migration and improved the photocatalytic performance of methylene blue. A V₂C/BVO composite catalyst prepared through a hydrothermal method can accelerate electron transfer and optimize hydrogen evolution reaction activity [17]. In addition, Pt/V₂C/Tx prepared by Wang et al. exhibited excellent activity and stability [18]. The above reports demonstrate that the study of V₂C MXene as a cocatalyst is promising for the development of semiconductor photocatalysts. However, the degradation of pollutants using V₂C MXene–modified g-C₃N₄ has not been previously investigated. Therefore, we explored the photocatalytic activity of g-C₃N₄@V₂C MXene photocatalyst and

applied it to the photocatalytic degradation of MO.

Herein, g-C₃N₄@V₂C MXene photocatalyst was synthesized using a simple self-assembly mixing technique and tested for their photocatalytic degradation efficiency toward MO under visible light. The g-C₃N₄@V₂C MXene photocatalyst exhibited higher charge transfer rates and electron-hole pair separation efficiencies than g-C₃N₄, considerably promoting the photocatalytic degradation of MO. A possible mechanism of the photocatalytic degradation of MO by g-C₃N₄@V₂C MXene photocatalyst was proposed based on the analysis of relevant experimental data. The study demonstrated that V₂C MXene is a cocatalyst with excellent performance and high potential for remedying water pollution.

2 Material and methods

2.1 Materials

Carbamide (H₂NCONH₂ ≥ 99%), tetramethylammonium hydroxide (TMAOH ≥ 25 wt%), and MO (C₁₄H₁₄O₃N₃SNa) were purchased from Aladdin. Hydrofluoric acid (HF) and ethanol (C₂H₅OH) were purchased from Xilong Chemical. MAX (V₂AlC) was purchased from Foshan Xinxu Technology Co., Ltd. Deionized (DI) water was prepared in a laboratory.

2.2 Catalyst synthesis

g-C₃N₄ was produced through a thermal polycondensation reaction with urea following a previously reported procedure [19]. First, 20 g of urea was dropped into a covered alumina crucible, which was then heated in a muffle furnace to 550°C at a heating rate of 2.5°C/min and maintained for 3 h at 550°C. After cooling to 25°C, the yellow solid formed in the crucible was ground into a fine powder.

V₂AlC (2 g) was added to 40 mL of 49% HF and mixed well to obtain a solution. The obtained solution was stirred for 24 h at 25°C and then for 48 h at 50°C to remove the aluminum layer. Then, 40 mL of 25-wt% TMAOH was added to the solution and stirred continuously for 24 h [20-22]. The agitated solution was centrifuged several times at 8000 rpm with ethanol and DI water until the pH approached neutral; it was then freeze-dried for 24 h to obtain V₂C MXene.

The self-assembly mixing technique was employed to synthesize g-C₃N₄@V₂C MXene photocatalyst. DI water (50 mL) was combined with 0.2 g of g-C₃N₄ and sonicated for 30 min; then, different masses of V₂C MXene were added to g-C₃N₄ and sonicated for 30 min. Finally, the homogeneous dispersion was obtained through magnetic stirring for 3 h [23]. The powder samples in the mixture were rinsed with DI water multiple times and dried for 24 h in a freeze-drying oven to obtain g-C₃N₄@V₂C MXene photocatalyst (referred to as g-C₃N₄@V₂C-X, X = 10, 20, and 30 mg). Fig. 1 shows the flowchart for the production of the g-C₃N₄@V₂C MXene

photocatalyst.

2.3 Characterization

The crystal structures of the photocatalysts were analyzed through X-ray diffraction (XRD, MiniFlex-600 from JEOL, Japan). The Fourier-transform infrared (FTIR) spectra of the photocatalysts were obtained using the Nicolet-6700 infrared spectrometer (Tokyo, Japan). The morphology and elemental contents of the prepared samples were examined using scanning electron microscopy (SEM, Czech TESCAN MIRA LMS) and X-ray energy-dispersive spectroscopy. The surfaces of the samples were analyzed via X-ray photoelectron spectroscopy (XPS, Thermo Scientific K-Alpha, USA). The lattice spacing of the samples was determined through high-resolution transmission electron microscopy (HRTEM, JEOL JEM 2100Plus, Tokyo, Japan). The photoluminescence (PL) spectra were obtained using FL/FS900 (Edinburgh, Cheadle). The ultraviolet–visible (UV–Vis) absorption spectra were measured using a PerkinElmer Lambda 750 spectrophotometer.

2.4 Electrochemical measurements

A standard three-electrode electrochemical workstation (CHI 660E) was used to measure transient photocurrent and electrochemical impedance. The electrolyte was Na_2SO_4 (0.2 M), and the light source was a xenon lamp (PLS-SXE300, 300 W). A platinum-sheet electrode served as the counter electrode, the standard calomel electrode (SCE) served as the reference electrode, and the sample served as the working electrode. To enable the deposition of the photocatalyst onto a fluorine-doped tin oxide (FTO) electrode to form a yellowish coating, the samples were dispersed in ethanol, water, and naphthalene sulfone to obtain a mixed solution. The mixed solution was then applied onto the FTO electrode using a pipette gun. Finally, the resultant FTO electrode was dried in an oven.

2.5 Photocatalytic degradation

The photocatalytic performance and stability of each sample were investigated using a xenon lamp (PLS-SXE300, 300 W) as a visible light source and an MO solution (10 mg/L) as a contaminant. In general, 50 mg of the photocatalyst was mixed well with 50 mL of the MO solution and stirred for 30 min in the dark to attain the adsorption–desorption equilibrium of MO molecules on the photocatalyst. Afterward, the solution was placed under the xenon lamp and 3.5 mL of the irradiated solution was taken at 0.5 h intervals. After the experiment, the suspended catalyst was filtered using a 220 nm polyethersulfone needle filter. UV–Vis spectroscopy was performed to detect numerical changes in the concentration of the target dyes.

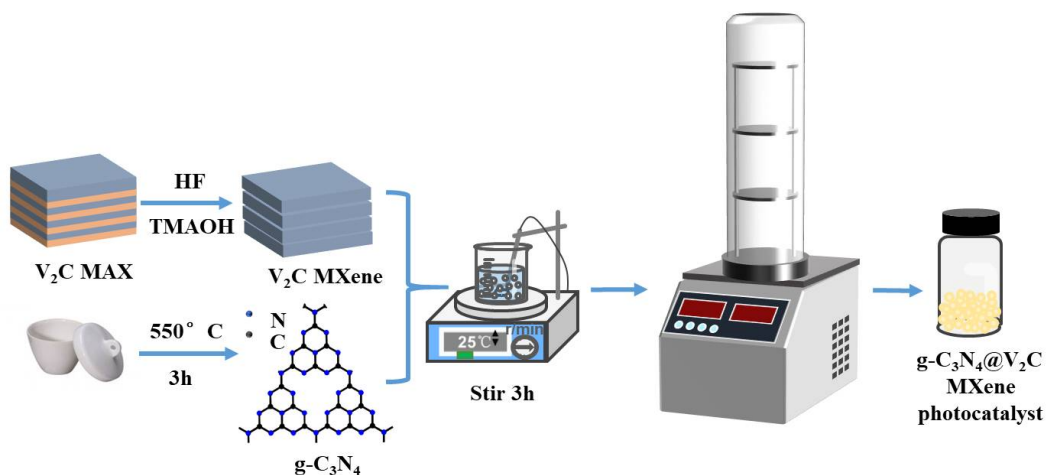


Fig. 1. Preparation of $g\text{-C}_3\text{N}_4@V_2\text{C}$ MXene photocatalyst.

3 Results and discussion

3.1 Morphological and structural analyses

Fig. 2 shows the SEM images of $g\text{-C}_3\text{N}_4$, $V_2\text{C}$, and $g\text{-C}_3\text{N}_4@V_2\text{C}$ -20 mg as well as elemental maps for $g\text{-C}_3\text{N}_4@V_2\text{C}$ -20 mg. The structure of $g\text{-C}_3\text{N}_4$ (Fig. 2a) is layered and agglomerated, which is typical for $g\text{-C}_3\text{N}_4$ prepared via thermal polycondensation [24]. Pure $V_2\text{C}$ MXene (Fig. 2b) exhibits a two-dimensional nanosheet-like structure. The lamellar structure of the aggregates does not substantially change after the addition of $V_2\text{C}$, proving that $V_2\text{C}$ MXene exhibits a negligible effect on the basic structure of $g\text{-C}_3\text{N}_4$. Moreover, the distributions of C, N, and V are fairly uniform in $g\text{-C}_3\text{N}_4@V_2\text{C}$ -20 mg (Figs. 2e–h). These results confirm the successful preparation of the $g\text{-C}_3\text{N}_4@V_2\text{C}$ MXene photocatalyst.

For further analysis, the prepared $g\text{-C}_3\text{N}_4@V_2\text{C}$ MXene photocatalyst were observed using HRTEM. Fig. 3 shows the HRTEM images of pure $g\text{-C}_3\text{N}_4$ and $g\text{-C}_3\text{N}_4@V_2\text{C}$ -20 mg. The $g\text{-C}_3\text{N}_4$ presented in Fig. 3a comprises multilayered nanosheets—a typical two-dimensional layered structure [25]. In particular, because of the special structure of $g\text{-C}_3\text{N}_4$, no considerable lattice stripes are observed in Fig. 3a. The HRTEM image of $g\text{-C}_3\text{N}_4@V_2\text{C}$ -20 mg (Fig. 3b) shows that $g\text{-C}_3\text{N}_4$ is in close contact with $V_2\text{C}$ MXene [26]. Moreover, the $V_2\text{C}$ MXene has three orientations with the same crystal spacing ($d = 0.15$ nm). This crystal plane spacing belongs to the (011) crystal plane of $V_2\text{C}$ MXene. Thus, HRTEM results verify that $V_2\text{C}$ MXene successfully modified $g\text{-C}_3\text{N}_4$.

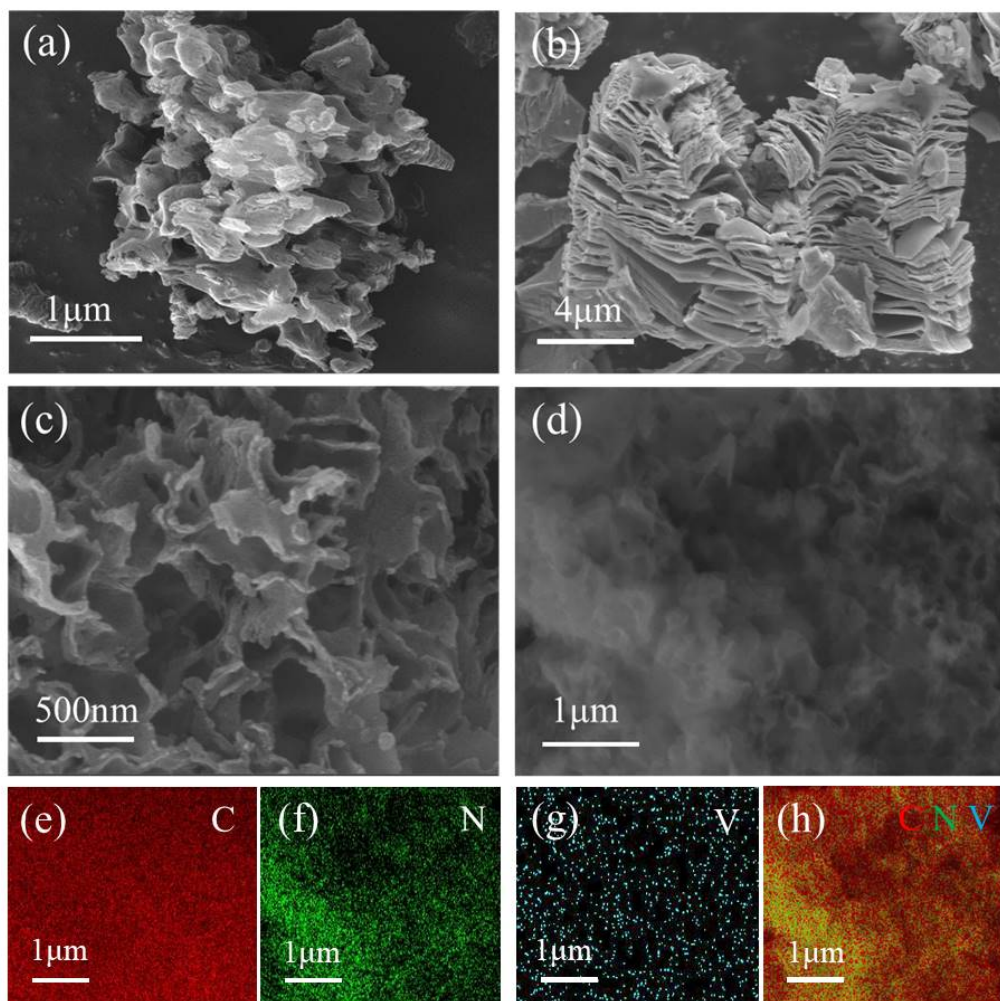


Fig. 2. SEM images of (a) g-C₃N₄, (b) V₂C MXene, and (c and d) g-C₃N₄@V₂C-20 mg. (e–h) Elemental maps of the C, N, and V in g-C₃N₄@V₂C-20 mg in selected regions of (d).

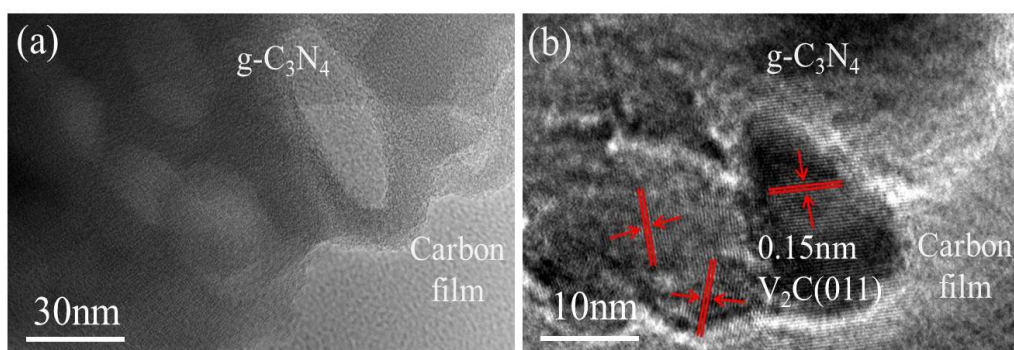


Fig. 3. HRTEM images of (a) g-C₃N₄ and (b) g-C₃N₄@V₂C-20 mg.

The crystal structures of g-C₃N₄, V₂C MXene, and g-C₃N₄@V₂C-20 mg were determined using XRD (Fig. 4a). Both g-C₃N₄ and g-C₃N₄@V₂C-20 mg show two strong peaks at 13.1° (100) and 27.3° (002), which were ascribed to the interlayer reflection of the tri-s-triazine unit and the interlayer stacking of the aromatic system, respectively [27]. Interestingly, the g-C₃N₄@V₂C MXene photocatalyst exhibits higher diffraction peak intensities and higher crystallinity compared to g-C₃N₄.

Compared to those of V_2AlC , the peaks of V_2C MXene are present at a lower angle and a new peak appears at 6.1° , confirming the successful preparation of V_2C MXene [28, 29]. Furthermore, the (010) crystal plane of V_2C MXene is present in the XRD pattern of $g-C_3N_4@V_2C-20$ mg. All peaks of pure $g-C_3N_4$ and V_2C MXene can be observed in the XRD pattern of $g-C_3N_4@V_2C-20$ mg, confirming the preparation of $g-C_3N_4@V_2C$ MXene photocatalyst. The XRD pattern of $g-C_3N_4@V_2C-20$ mg (Fig. 4c) is essentially unaltered after cycling, and some distinctive peaks are also quite visible, indicating that the materials are very stable.

The surface groups of V_2C MXene, $g-C_3N_4$, and $g-C_3N_4@V_2C-20$ mg were analyzed using FTIR (Fig. 4d). Both pure $g-C_3N_4$ and $g-C_3N_4@V_2C-20$ mg exhibit three identical characteristic absorption peaks at $2970\sim 3410\text{ cm}^{-1}$, $1205\sim 1690\text{ cm}^{-1}$, and $\sim 815\text{ cm}^{-1}$, which were ascribed to the vibrational absorption of the NH_x group, the conjugated CN heterocycle, and the tri-s-triazine unit, respectively [30]. No additional V_2C MXene characteristic peaks are identified in the XRD pattern of $g-C_3N_4@V_2C-20$ mg except at $\sim 2350\text{ cm}^{-1}$, which was attributed to the low mass fraction of V_2C MXene and the overlap of these peaks at 1600 and 760 cm^{-1} with the vibration/stretching mode of $g-C_3N_4$. In summary, the characteristic absorption peaks of $g-C_3N_4$ and $g-C_3N_4@V_2C-20$ mg are comparable, indicating that the introduction of a moderate quantity of V_2C MXene does not affect the surface groups of $g-C_3N_4$.

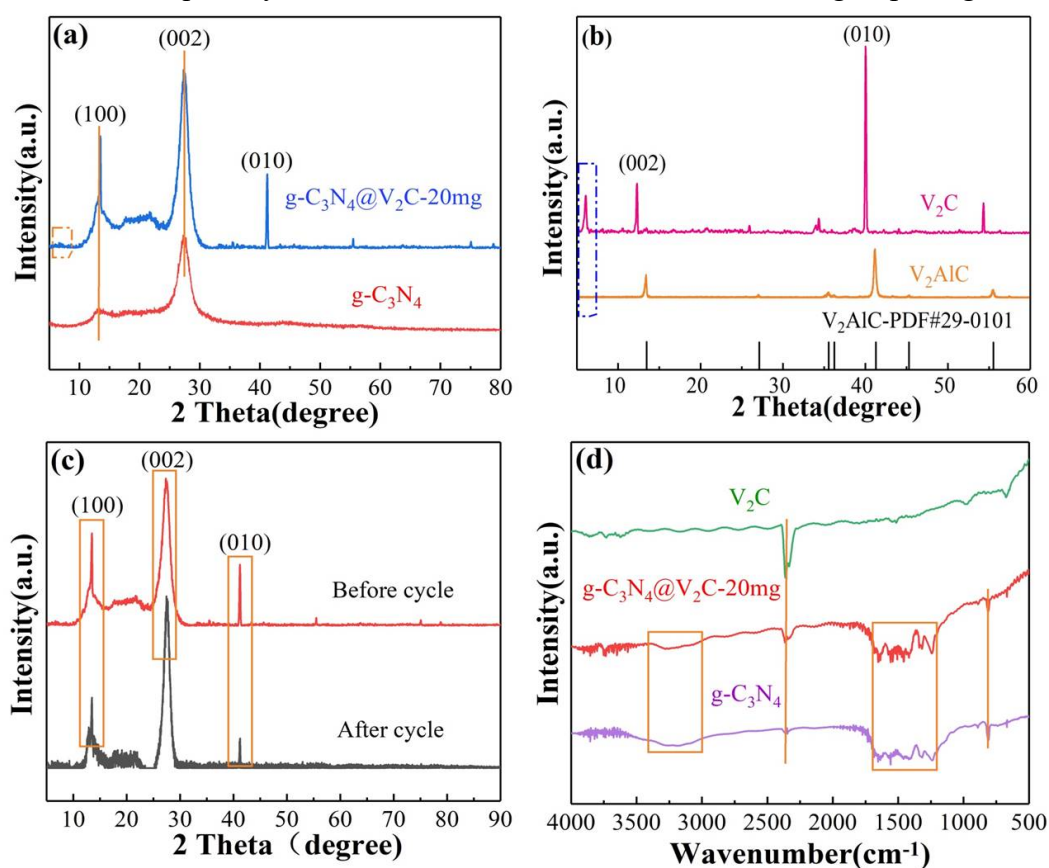


Fig. 4. XRD patterns of (a) $g-C_3N_4$ and $g-C_3N_4@V_2C-20$ mg, (b) V_2C MXene and V_2AlC MAX, and (c) $g-C_3N_4@V_2C-20$ mg (before and after cycling). (d) FTIR spectra of V_2C MXene, $g-C_3N_4$, and $g-C_3N_4@V_2C-20$ mg.

The chemical composition of the photocatalysts was determined through XPS.

The XPS spectra of the g-C₃N₄@V₂C MXene photocatalyst (Fig. 5a) shows distinct C, N, and O peaks, where the O peak is probably due to H₂O/oxidation-generated oxides adsorbed on the sample surface. The absence of a V characteristic peak in the XPS spectrum of g-C₃N₄@V₂C-20 mg was attributed to the low amount of V₂C, resulting in an inconsequential V peak. The three major peaks in the C1s spectrum (Fig. 5b) at 284.8 (C=C), 286.5 (C-NH_x), and 288.2 eV (N=C-N₂) on the C 1s spectrum are ascribed to the aromatic ring, sp³-coordinated carbon bond, and sp²-hybridized carbon atom, respectively. The four binding energy peaks in the N1s spectrum (Fig. 5c) at 398.5 (C-N=C), 399.9 (N-C₃), 401.0 (C-NH₂), and 404.6 eV were ascribed to sp²-hybridized N, graphitic N, amino, and excitation, respectively [31]. The five peaks shown in Fig. 5d correspond to different oxidation states of V. The V⁵⁺ peak at 517.5 eV has the second-highest intensity. The two peaks in the V2p spectrum at 520.6 and 516.4 eV were attributed to V⁴⁺. Finally, two V³⁺ peaks are observed at 514.9 and 513.6 eV [32].

Compared with those of g-C₃N₄, some peaks of g-C₃N₄@V₂C-20 mg are displaced. Considerable displacement (dashed portion) of the peaks implies that V₂C MXene and g-C₃N₄ have a strong surface interaction. Compared to those in g-C₃N₄, the C1s and N1s in the composite migrate to higher energy levels, indicating that g-C₃N₄ is an electron donor and V₂C MXene is an electron acceptor [33]. Thus, V₂C MXene exhibits excellent electron trapping ability. The XPS results demonstrate that V₂C MXene is an efficient cocatalyst and can promote the rapid movement of photogenerated electrons from g-C₃N₄ to V₂C MXene and enhance the visible-light photocatalytic performance.

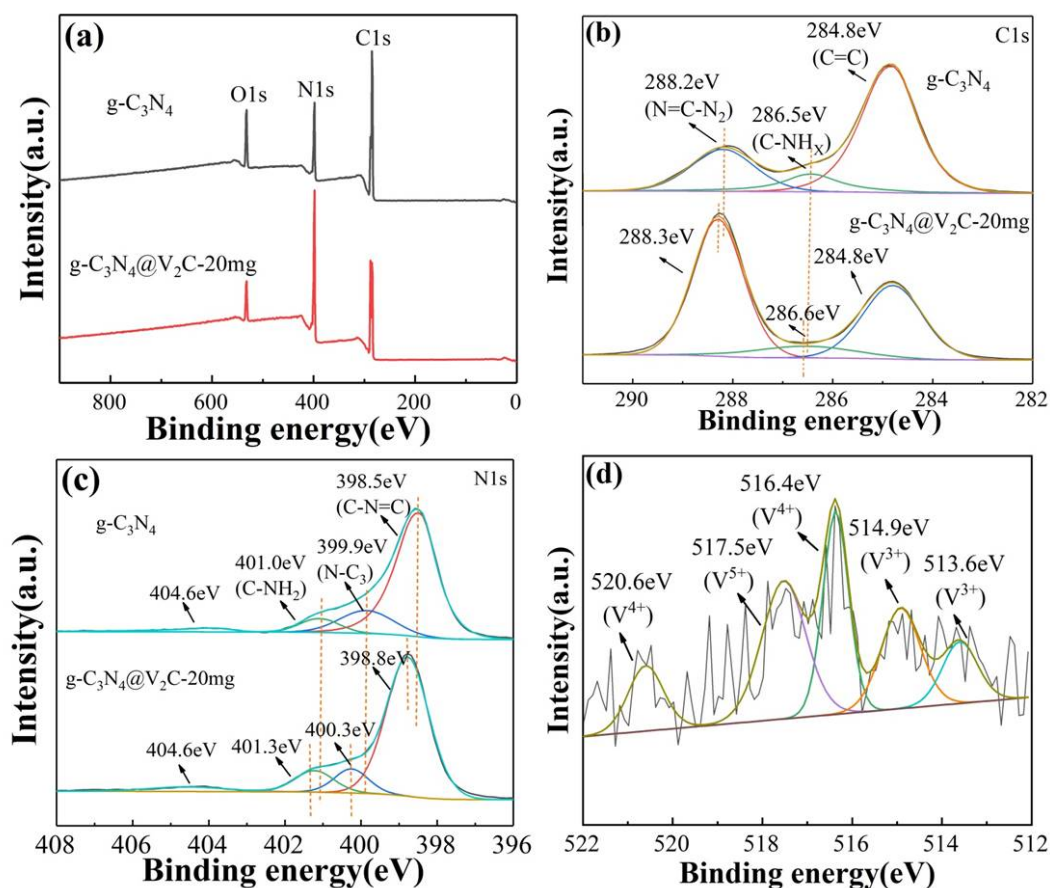


Fig. 5. (a) XPS spectra, (b) C1s high-resolution spectra, and (c) N1 high-resolution spectra of g-C₃N₄ and g-C₃N₄@V₂C-20 mg. (d) V2p high-resolution XPS spectrum of g-C₃N₄@V₂C-20 mg.

3.2 Bandgap and optoelectronic characterization

Fig. 6a presents the UV–Vis absorption spectra of V₂C MXene, g-C₃N₄, and g-C₃N₄@V₂C-20 mg. The absorption edges of g-C₃N₄@V₂C-20 mg and pure g-C₃N₄ are clearly visible at 440 nm. The composite exhibits improved absorption properties in ultraviolet and visible regions, which was attributed to the broadband absorption of V₂C MXene across the solar spectrum. Moreover, the absorbance of g-C₃N₄@V₂C-20 mg is approximately two times higher than that of g-C₃N₄ under visible light (450–800 nm). Obtained through the Tauc-function bandgap simulation, the bandgaps of g-C₃N₄ and g-C₃N₄@V₂C-20 mg are 2.84 and 2.82 eV, respectively (Fig. 6b) [34]. The g-C₃N₄@V₂C-20 mg composite can absorb a greater range of wavelengths in the visible spectrum because of the narrower bandgap, suggesting that it may enhance the photocatalytic degradation efficiency of MO. Zhang et al. reported that V₂C MXene with –F and –OH end groups is a narrow-bandgap semiconductor. Thus, we determined that the bandgap of V₂C MXene is 0.42 eV (Fig. 6c) [35].

Fig. 6d presents the electrochemical impedance spectra of different photocatalysts. Overall, the smaller the arc radius, the smaller the impedance of charge transfer and the higher the charge transfer rate of the photocatalyst. Evidently, g-C₃N₄@V₂C-20 mg exhibits a lower arc radius than g-C₃N₄. The steady-state PL spectra and transient photocurrent response of g-C₃N₄@V₂C-20 mg and g-C₃N₄ were further measured to investigate the electron–hole pair separation efficiency and transport efficiency of the composite. As shown in Fig. 6e, under 350-nm excitation, both g-C₃N₄@V₂C MXene photocatalyst and g-C₃N₄ exhibit an emission peak at 470 nm. Notably, the peak intensity of g-C₃N₄@V₂C-20 mg is lower, suggesting that the electron–hole pair recombination frequency of the g-C₃N₄@V₂C-20 mg photocatalyst is lower and the number of photogenerated carriers is higher than those of g-C₃N₄. Additionally, after the addition of V₂C MXene, the photocurrent of the composites substantially increases, implying that g-C₃N₄@V₂C-20 mg exhibits considerably better photogenerated carrier separation capacity (Fig. 6f) [36].

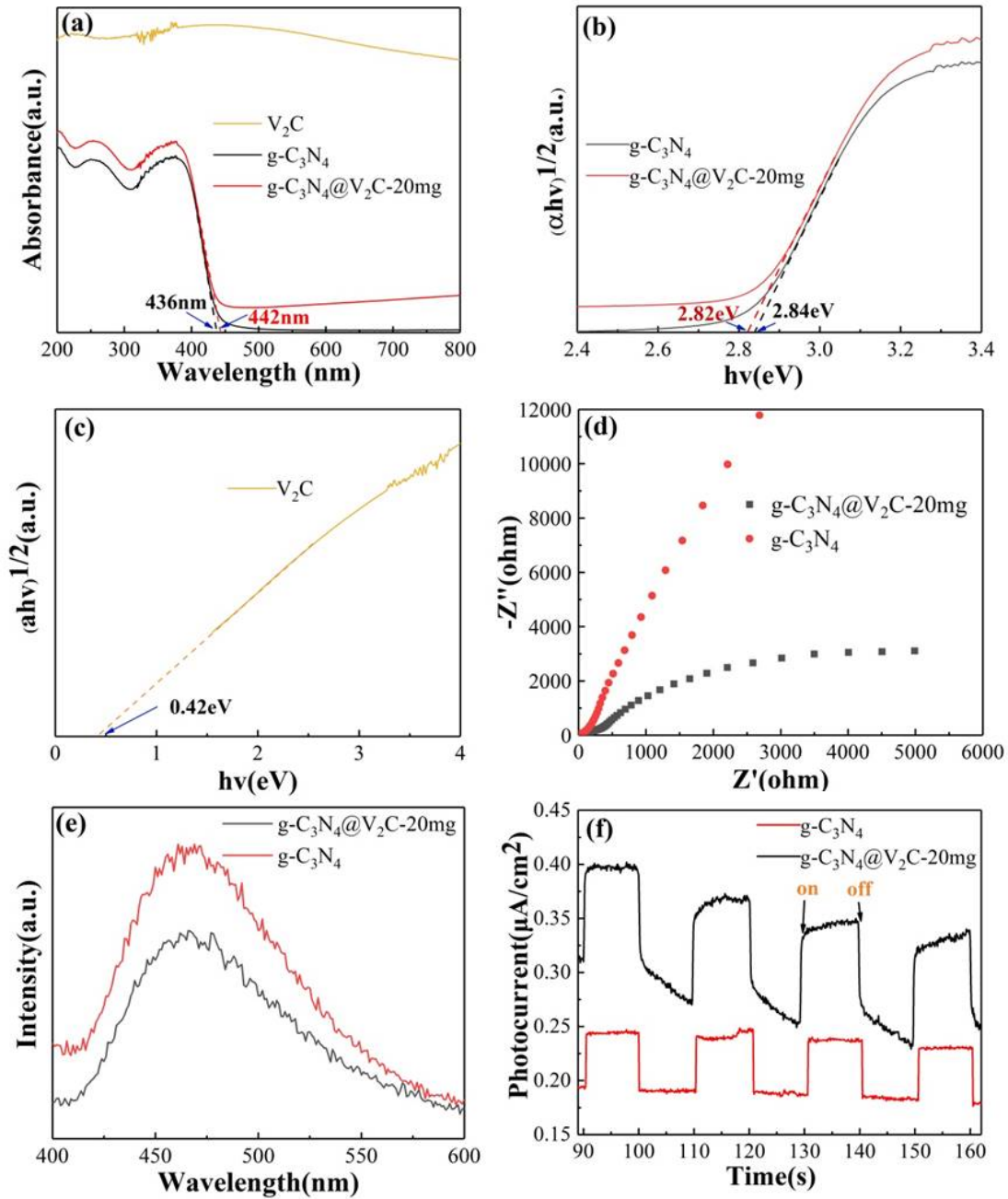


Fig. 6. (a–c) UV–Vis absorption spectra and Tauc-function bandgap simulations of g-C₃N₄, V₂C MXene, and g-C₃N₄@V₂C-20 mg. (d–f) Electrochemical impedance spectra, steady-state PL spectra, and photocurrent responses of g-C₃N₄ and g-C₃N₄@V₂C-20 mg.

3.3 Photocatalytic performance

The photocatalytic performances of V₂C MXene, g-C₃N₄, and g-C₃N₄@V₂C-X were investigated for different MO concentrations using a 300 W xenon lamp (Fig. 7a). The degradation efficiency was defined as $\eta = (C_0 - C) / C_0$, where C_0 represents the initial MO concentration and C represents the MO concentration at time t . For each photocatalyst, three sets of parallel experiments were performed, and the

data from the three sets of experiments were acquired and averaged, and this average value was utilized for graphing. The error value is the difference between the three values and the average. As shown in Fig. 7a, the concentration of MO negligibly changes when using pure V₂C MXene. The degradation efficiency of MO by g-C₃N₄ is 60.4% after irradiation for 120 min. The MO degradation efficiency of g-C₃N₄@V₂C-10 mg, g-C₃N₄@V₂C-20 mg, and g-C₃N₄@V₂C-30 mg are 86.6%, 94.5%, and 88.8%, respectively, after irradiation for 120 min. The degradation efficiency of the g-C₃N₄@V₂C MXene photocatalyst is 34.1% higher than that of g-C₃N₄. The contact between V₂C MXene and g-C₃N₄ at a low amount of V₂C MXene is not sufficient to produce a substantial number of exposed active centers and decrease the carrier separation efficiency. At the same time, an excessive amount of V₂C MXene absorbs an excessive amount of visible light, constraining the effective light contact area of g-C₃N₄ and preventing the generation of a sufficient amount of photogenerated carriers in g-C₃N₄ to maintain an effective contact with dye molecules, thus reducing the photocatalytic efficiency. Therefore, the introduction of an appropriate amount of V₂C MXene results in a high photocatalytic degradation efficiency of the photocatalyst.

The kinetic behavior of the degradation reaction may be expressed using the first-order kinetic equation— $\ln(C/C_0) = kt$, where k and t are the rate constant of the photocatalytic degradation process and time of illumination, respectively. The k values for V₂C, g-C₃N₄, g-C₃N₄@V₂C-10 mg, g-C₃N₄@V₂C-20 mg, and g-C₃N₄@V₂C-30 mg were 0.0012, 0.00756, 0.01659, 0.02475, and 0.01936 min⁻¹, respectively. The g-C₃N₄@V₂C-20 mg photocatalyst shows the highest k of 0.02475min⁻¹, which is 3.3 times higher than that of g-C₃N₄. At the same time, the k values of g-C₃N₄@V₂C-10 mg and g-C₃N₄@V₂C-30 mg are 2.2 and 2.6 times, respectively, higher than that of g-C₃N₄. These results further confirm that V₂C MXene is a promising cocatalyst for the photocatalytic degradation of dyes.

In addition to good photocatalytic degradation performance, a promising photocatalyst must also exhibit a certain degree of stability. After three repeated cycles (Fig. 7c), the photocatalytic degradation performance of MO by the g-C₃N₄@V₂C-20 mg catalyst did not considerably change and remained above 85%. Thus, the g-C₃N₄@V₂C MXene photocatalyst has excellent photocatalytic performance and cycling stability. Moreover, as compared to other g-C₃N₄-based photocatalysts, the g-C₃N₄@V₂C MXene photocatalyst in this work also had greater photocatalytic ability. The V₂C MXene material is a potential co-catalyst for the photocatalytic degradation of dyes, which can be further substantiated based on this information.

To further investigate the mechanism through which the g-C₃N₄@V₂C MXene photocatalyst promotes the degradation of pollutants (MO), radical trapping tests were performed on the g-C₃N₄@V₂C MXene photocatalyst. The following compounds were used as scavengers of superoxide radicals ($\cdot\text{O}_2^-$), holes (h^+), electrons (e^-), and hydroxyl radicals ($\cdot\text{OH}$): benzoquinone (BQ), potassium iodide (KI), potassium dichromate (K₂Cr₂O₇), and isopropanol (IPA), respectively [37]. The MO without added free radical scavengers was almost completely degraded. As shown in Fig. 7d,

the C/C_0 without the addition of radical scavengers is 0.055. After the addition of BQ, the photocatalytic performance decreased by approximately 80%, thus demonstrating that $\cdot O_2^-$ is the primary active group in the degradation process. The C/C_0 after the addition of four other free radical scavengers—BQ, KI, $Kr_2Cr_2O_7$, and IPA—are 0.9, 0.42, 0.35, and 0.29, respectively. Therefore, the addition of KI, $Kr_2Cr_2O_7$, and IPA also inhibited the photocatalytic degradation of MO by the composites, indicating that h^+ , e^- , and $\cdot OH$ are also active groups in the photocatalytic degradation. Based on the above results, the degree of action of the active groups is $\cdot O_2^- > h^+ > e^- > \cdot OH$.

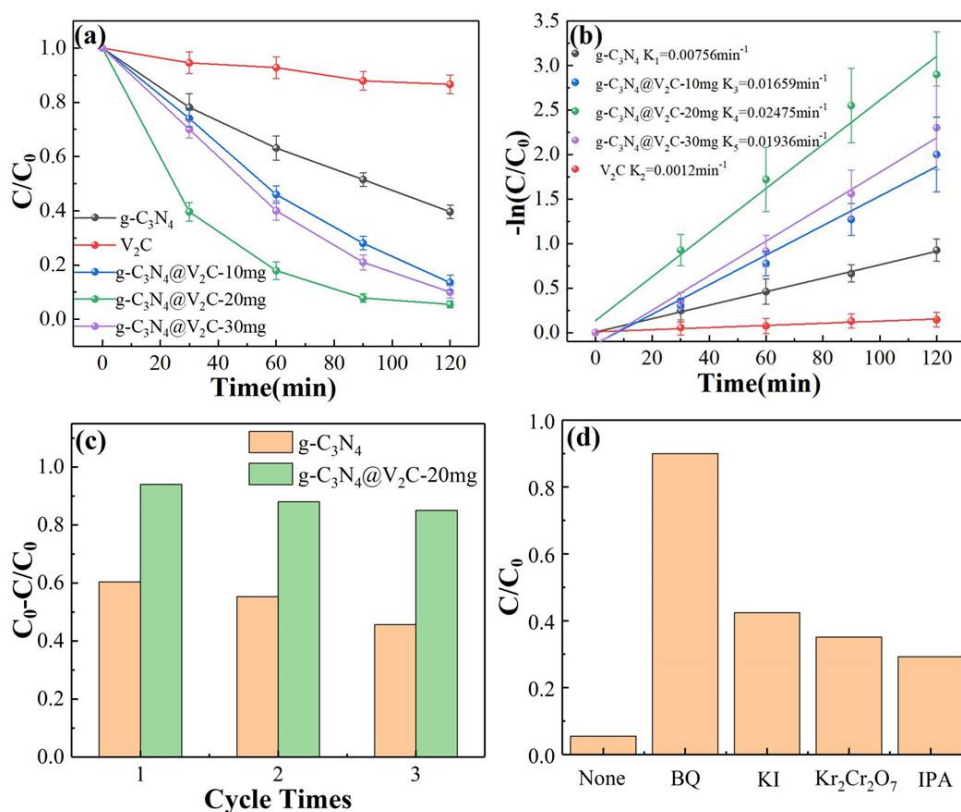


Fig. 7. (a) Photocatalytic degradation by $g-C_3N_4$, V_2C MXene, $g-C_3N_4@V_2C-10$ mg, $g-C_3N_4@V_2C-20$ mg, and $g-C_3N_4@V_2C-30$ mg under visible light (C and C_0 are MO concentrations after and before irradiation, respectively); (b) degradation kinetics of $g-C_3N_4$, V_2C MXene, $g-C_3N_4@V_2C-10$ mg, $g-C_3N_4@V_2C-20$ mg, and $g-C_3N_4@V_2C-30$ mg under visible light; (c) cycling stability of $g-C_3N_4$ and $g-C_3N_4@V_2C-20$ mg in MO degradation under visible light; and (d) effect of different radical scavengers on the photocatalytic degradation by $g-C_3N_4@V_2C-20$ mg.

Table 1. Comparison of photocatalytic degradation efficiency of MO with different $g-C_3N_4$ -based photocatalysts.

Photocatalysts	Light	Degradation rate (%)	Time (min)	Pollutants	Reference
----------------	-------	----------------------	------------	------------	-----------

g-C ₃ N ₄ @V ₂ C-20mg	Vis	94.5	120	MO	This
BN/g-C ₃ N ₄	Vis	80	90	MO	[38]
g-C ₃ N ₄ /Ag/P ₃ HT	Vis	75	480	MO	[39]
Fe(III)-C ₃ N ₄	Vis	80	70	MO	[40]
GCN-3/VL/PDS	Vis	89.6	40	MO	[41]
ZnO HC@Ti ₃ C ₂	Vis	87.8	60	MO	[42]
MF-MXene/ppy	Vis	91.75	240	MO	[43]

3.4 Possible photocatalytic mechanisms

The Mott–Schottky curve can be used for obtaining the flat-band potential (E_{fb}) of semiconductors. The intercept of the straight line with the horizontal axis is E_{fb} , which is considered the Fermi energy level. If the Fermi energy level is near the edge of the energy band, the obtained E_{fb} can be considered an extreme value of the conduction band (E_{CB} , n-type) or valence band (E_{VB} , p-type) [44]. As shown in Fig. 8, g-C₃N₄, V₂C MXene, and g-C₃N₄@V₂C-20 mg exhibit positive slopes and are n-type semiconductors. With SCE as the reference electrode, the intersections of the approximated straight line with the horizontal axis for g-C₃N₄, V₂C MXene, and g-C₃N₄@V₂C-20 mg are -1.50 , -1.29 , and -1.36 eV, respectively. The SCE deviation is 0.24 eV compared to the standard hydrogen electrode. Thus, the E_{CB} of g-C₃N₄, V₂C MXene, and g-C₃N₄@V₂C-20 mg have the following values: -1.26 , -1.05 , and -1.12 eV, respectively. Using empirical Equation (1), the E_{CB} and E_{VB} of a semiconductor can be obtained [45]. The determined E_{VB} of g-C₃N₄, V₂C MXene, and g-C₃N₄@V₂C-20 mg are 1.58, -0.63 , and 1.70 eV, respectively.

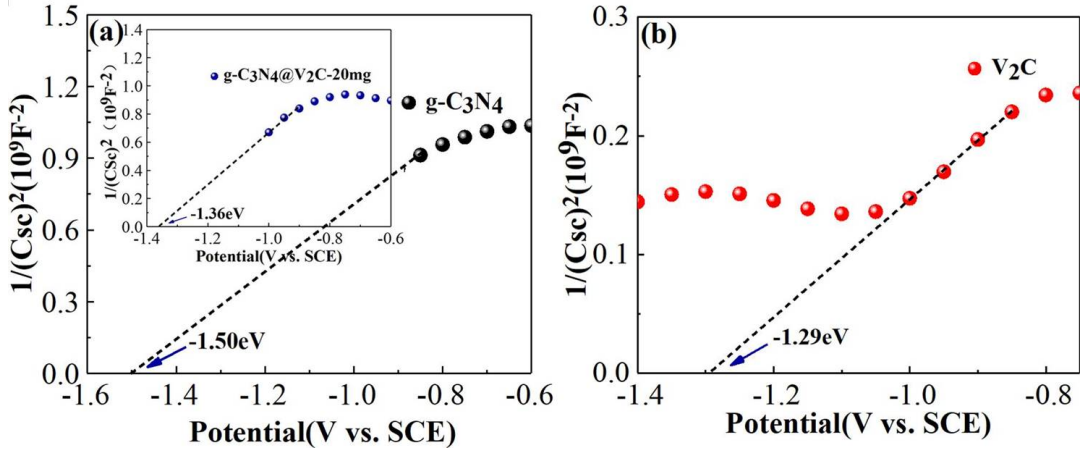
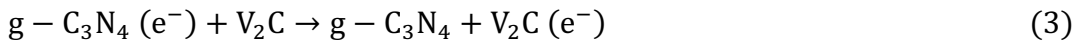
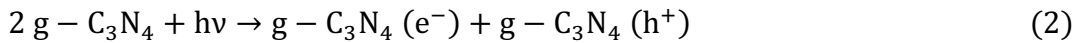
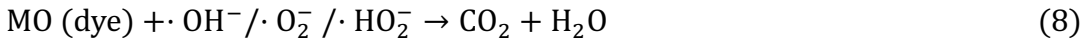
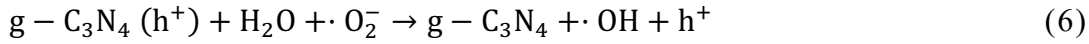


Fig. 8. Mott–Schottky curves for (a) g-C₃N₄ (the inset corresponds to g-C₃N₄@V₂C-20 mg) and (b) V₂C MXene.

$$E_{VB} = E_g + E_{CB} \quad (1)$$





Based on the theoretical analysis and characterization tests, a rational photocatalytic mechanism was suggested to illustrate the photocatalytic process of g-C₃N₄@V₂C MXene photocatalyst on MO. Empirical equations (2)–(8) describe the conversion and formation of different active groups of g-C₃N₄@V₂C MXene photocatalyst throughout photocatalytic degradation [46]. Fig. 9 illustrates how g-C₃N₄ generates photocarriers after absorbing visible light. Electrons (e⁻) are transferred from the valence band (E_{VB}) to conduction band (E_{CB}), but the photocatalytic efficiency is hampered by quick recombination of a substantial number of electron–hole pairs at this time. When V₂C MXene and g-C₃N₄ are tightly connected, V₂C MXene acts as an electron acceptor at the better band edge position and acts as a cocatalyst in the photocatalytic degradation of pollutants (MO). Therefore, less recombination occurs between the photogenerated carriers (e⁻–h⁺), and a substantial number of electrons (e⁻) rapidly migrate from the g-C₃N₄ conduction band (E_{CB}) to V₂C MXene. These photogenerated electrons that have migrated could subsequently interact with organic molecules to produce CO₂ and ·OH. In addition, the band edge of MXene is lower than the band edge of ·O₂⁻ (-0.33 eV), facilitating the excitation and production of superoxide radicals (·O₂⁻). The valence band (E_{VB}) of g-C₃N₄ is higher than that of ·OH/OH⁻ (2.29 eV). Thus, some of the generated ·O₂⁻ react with H⁺ to produce ·OH/OH⁻ [47]. Finally, these active groups (·OH/·O₂⁻) bind to MO molecules and degrade them to produce CO₂.

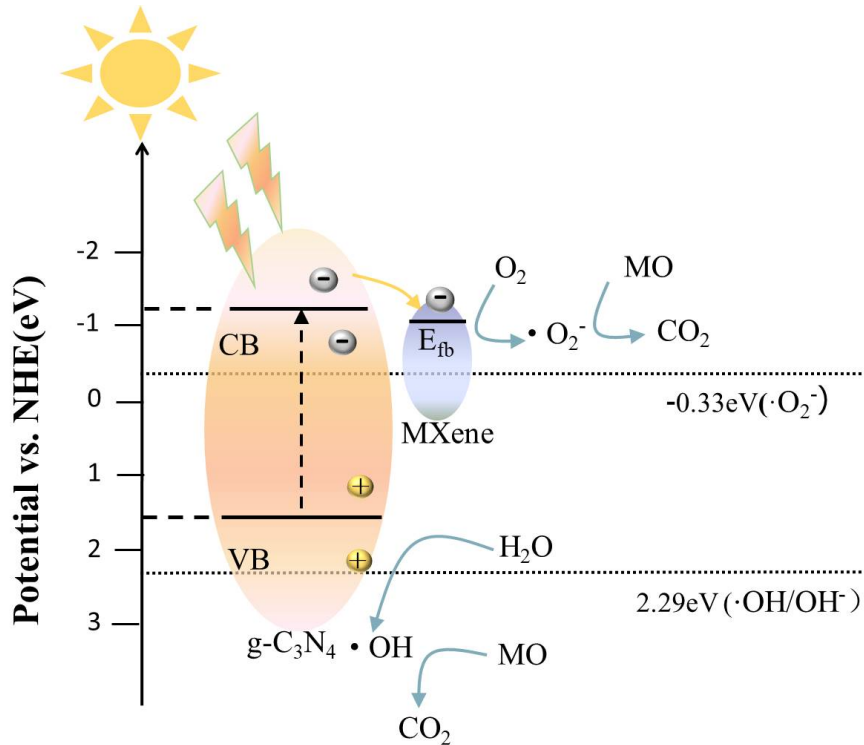


Fig. 9. Degradation mechanism by g-C₃N₄@V₂C MXene photocatalyst under visible light.

4 Conclusions

Herein, a novel photocatalyst with a closely connected interface, g-C₃N₄@V₂C MXene photocatalyst, was synthesized through modification of g-C₃N₄ with V₂C MXene. The degradation efficiency of MO by the g-C₃N₄@V₂C-20 mg composite is up to 94.5% after 120 min of exposure to visible light. The g-C₃N₄@V₂C MXene photocatalyst can swiftly transfer photogenerated electrons (e⁻) from g-C₃N₄ to V₂C MXene, restrain the rapid recombination between electrons and holes (e⁻-h⁺), cause participation of a substantial number of photogenerated carriers in subsequent oxidation–reduction, and promote the photocatalytic degradation of MO. Moreover, the cycling experiment demonstrated the outstanding photocatalytic activity and cycling stability of g-C₃N₄@V₂C MXene photocatalyst. This work confirms that V₂C MXene is an excellent cocatalyst for degrading dyes in water and provides a new perspective for designing g-C₃N₄-based photocatalysts.

CRedit authorship contribution statement

Ruizheng Xu: Investigation, Formal analysis, Writing – original draft. **Guiyu Wei:** Formal analysis. **Zhemin Xie:** Data curation. **Sijie Diao:** Investigation. **Jianfeng Wen:** Conceptualization, Funding acquisition. **Tao Tang:** Funding acquisition, Resources. **Li Jiang:** Supervision. **Ming Li:** Supervision, Writing – review & editing. **Guanghui Hu:** Writing – review & editing.

Declaration of Competing Interest

The authors declare that they have no known competing financial interests or personal relationships that could have appeared to influence the work reported in this paper.

Declaration of generative AI and AI-assisted technologies in the

writing process

All authors of this thesis did not use generative artificial intelligence (AI) or AI-assisted technologies in the writing process.

Acknowledgments

This work was financially supported by the National Natural Science Foundation of China (12164013), the Natural Science Foundation of Guangxi Province (2020GXNSFBA297125), the Science and Technology Base and Talent Special Project of Guangxi Province (AD21220029), Research Foundation of Guilin University of Technology (GUTQDJJ2019011).

References

- [1] F. Wang, Q. Li, D. Xu, Recent Progress in Semiconductor-Based Nanocomposite Photocatalysts for Solar-to-Chemical Energy Conversion, *Adv. Energy Mater.* 7 (2017) 1700529.
- [2] M. Wang, Z. Cui, M. Yang, L. Lin, X. Chen, M. Wang, J. Han, Core/shell structured CdS/polydopamine/TiO₂ ternary hybrids as highly active visible-light photocatalysis, *J. Colloid Interf. Sci.* 544 (2019) 1-7.
- [3] J. Ning, J. Zhang, R. Dai, Q. Wu, L. Zhang, W. Zhang, J. Yan, F. Zhang, Experiment and DFT study on the photocatalytic properties of La-doped Bi₂WO₆ nanoplate-like materials, *Appl. Surf. Sci.* 579 (2022) 152219.
- [4] Y. Wang, G. Tan, T. Liu, Y. Su, H. Ren, X. Zhang, A. Xia, L. Lv, Y. Liu, Photocatalytic properties of the g-C₃N₄/010 facets BiVO₄ interface Z-Scheme photocatalysts induced by BiVO₄ surface heterojunction, *Appl. Catal. B Environ.* 234 (2018) 37-49.
- [5] J.W. Fu, J.G. Yu, C.J. Jiang, B. Cheng, g-C₃N₄-Based Heterostructured Photocatalysts, *Adv. Energy Mater.* 8 (2018) 31.
- [6] Q. Zhu, Z. Xu, B. Qiu, M. Xing, J. Zhang, Emerging Cocatalysts on g-C₃N₄ for Photocatalytic Hydrogen Evolution, *Small* 17 (2021) 2101070.
- [7] D. Jiang, B. Wen, Q. Xu, M. Gao, D. Li, M. Chen, Plasmonic Au Nanoparticles/KCa₂Nb₃O₁₀ nanosheets 0D/2D heterojunctions with enhanced photocatalytic activity towards the degradation of tetracycline hydrochloride, *J. Alloy. Compd.* 762 (2018) 38-45.
- [8] H.-Y. Phin, Y.-T. Ong, J.-C. Sin, Effect of carbon nanotubes loading on the photocatalytic activity of zinc oxide/carbon nanotubes photocatalyst synthesized via a modified sol-gel method, *J. Environ. Chem. Eng.* 8 (2020) 103222.
- [9] T. Xu, D. Wang, L. Dong, H. Shen, W. Lu, W. Che, Graphitic carbon nitride co-modified by zinc phthalocyanine and graphene quantum dots for the efficient photocatalytic degradation of refractory contaminants, *Appl. Catal. B Environ.* 244 (2019) 96-106.
- [10] A. Yuan, H. Lei, F. Xi, J. Liu, L. Qin, Z. Chen, X. Dong, Graphene quantum dots decorated graphitic carbon nitride nanorods for photocatalytic removal of antibiotics, *J. Colloid Interf. Sci.* 548 (2019) 56-65.
- [11] B. Sun, P. Qiu, Z. Liang, Y. Xue, X. Zhang, L. Yang, H. Cui, J. Tian, The fabrication of 1D/2D CdS nanorod@Ti₃C₂ MXene composites for good photocatalytic activity of hydrogen generation and ammonia synthesis, *Chem. Eng. J.* 406 (2021) 127177.
- [12] H. Tian, M. Liu, W. Zheng, Constructing 2D graphitic carbon nitride nanosheets/layered MoS₂/graphene ternary nanojunction with enhanced photocatalytic activity, *Appl. Catal. B Environ.* 225 (2018) 468-476.
- [13] W. Zhang, Y. Ma, X. Zhu, S. Liu, T. An, J. Bao, X. Hu, H. Tian, Fabrication of Ag decorated g-C₃N₄/LaFeO₃ Z-scheme heterojunction as highly efficient visible-light photocatalyst for degradation of methylene blue and tetracycline hydrochloride, *J. Alloy. Compd.* 864 (2021) 158914.
- [14] J. Bao, X. Jiang, L. Huang, W. Quan, C. Zhang, Y. Wang, H. Wang, Y. Zeng, W. Zhang, Y. Ma, S. Yu, X. Hu, H. Tian, Molybdenum disulfide loading on a Z-scheme graphitic carbon nitride and lanthanum nickelate heterojunction for enhanced photocatalysis: Interfacial charge transfer and mechanistic insights, *J. Colloid Interf. Sci.* 611 (2022) 684-694.
- [15] W. Zhou, B. Yu, J. Zhu, K. Li, S. Tian, Enhanced photocatalytic activities of a hierarchical ZnO/V₂C MXene hybrid with a close coupling heterojunction for the degradation of methyl orange, phenol and methylene blue dye, *New J. Chem.* 46 (2022) 14793-14804.

- [16] W. Zhou, B. Yu, J. Zhu, K. Li, S. Tian, Hierarchical ZnO/MXene (Nb₂C and V₂C) heterostructure with efficient electron transfer for enhanced photocatalytic activity, *Appl. Surf. Sci.* 590 (2022) 153095.
- [17] S. Akir, J. Azadmanjiri, N. Antonatos, L. Dekanovsky, P.K. Roy, V. Mazanek, R. Lontio Fomekong, J. Regner, Z. Sofer, Atomic-layered V₂C MXene containing bismuth elements: 2D/0D and 2D/2D nanoarchitectonics for hydrogen evolution and nitrogen reduction reaction, *Nanoscale* (2023).
- [18] J. Wang, Y. Guan, Q. Zhang, H. Zhu, X. Li, Y. Li, Z. Dong, G. Yuan, Y. Cong, Well-dispersed ultrafine Pt nanoparticles anchored on oxygen-rich surface of V₂CT (MXene) for boosting hydrogen evolution reaction, *Appl. Surf. Sci.* 582 (2022) 152481.
- [19] Q.Z. Tao, R.Z. Xi, L. Chang, Q.C. Yan, D.L. Ai, A facile route to prepare TiO₂/g-C₃N₄ nanocomposite photocatalysts by atomic layer deposition, *J. Alloy. Compd.* 855 (2021) 157446.
- [20] D. Huang, Y. Xie, D. Lu, Z. Wang, J. Wang, H. Yu, H. Zhang, Demonstration of a White Laser with V₂C MXene-Based Quantum Dots, *Adv. Mater.* 31 (2019) 1901117.
- [21] P. Kuang, J. Low, B. Cheng, J. Yu, J. Fan, MXene-based photocatalysts, *J. Mater. Sci. Technol.* 56 (2020) 18-44.
- [22] J. Xuan, Z. Wang, Y. Chen, D. Liang, L. Cheng, X. Yang, Z. Liu, R. Ma, T. Sasaki, F. Geng, Organic-Base-Driven Intercalation and Delamination for the Production of Functionalized Titanium Carbide Nanosheets with Superior Photothermal Therapeutic Performance, *Angew. Chem.* 128 (2016) 14789-14794.
- [23] Y. Li, L. Ding, Y. Guo, Z. Liang, H. Cui, J. Tian, Boosting the Photocatalytic Ability of g-C₃N₄ for Hydrogen Production by Ti₃C₂ MXene Quantum Dots, *ACS Appl. Mater. Interfaces* 11 (2019) 41440-41447.
- [24] F. Guo, L. Wang, H. Sun, M. Li, W. Shi, High-efficiency photocatalytic water splitting by a N-doped porous g-C₃N₄ nanosheet polymer photocatalyst derived from urea and N,N-dimethylformamide, *Inorg. Chem. Front.* 7 (2020) 1770-1779.
- [25] P. Qiu, Z. Liang, X. Liu, X. Qian, H. Cui, J. Tian, Synthesis of salicylic acid-modified graphite carbon nitride for enhancing photocatalytic nitrogen fixation, *J. Colloid Interf. Sci.* 571 (2020) 318-325.
- [26] M. Yu, H. Liang, R. Zhan, L. Xu, J. Niu, Sm-doped g-C₃N₄/Ti₃C₂ MXene heterojunction for visible-light photocatalytic degradation of ciprofloxacin, *Chinese Chem. Lett.* 32 (2021) 2155-2158.
- [27] Y. Zhu, Z. Chen, Y. Gao, C. Hu, General synthesis of carbon and oxygen dual-doped graphitic carbon nitride via copolymerization for non-photochemical oxidation of organic pollutant, *J. Hazard. Mater.* 394 (2020) 122578.
- [28] M. Xu, T. Wu, J. Qi, D. Zhou, Z. Xiao, V₂C/VO₂ nanoribbon intertwined nanosheet dual heterostructure for highly flexible and robust lithium-sulfur batteries, *J. Mater. Chem. A.* 9 (2021) 21429-21439.
- [29] G. Zuo, Y. Wang, W.L. Teo, A. Xie, Y. Guo, Y. Dai, W. Zhou, D. Jana, Q. Xian, W. Dong, Y. Zhao, Enhanced photocatalytic water oxidation by hierarchical 2D-Bi₂MoO₆@2D-MXene Schottky junction nanohybrid, *Chem. Eng. J.* 403 (2021) 126328.
- [30] Y. Liang, X. Wang, W. An, Y. Li, J. Hu, W. Cui, A g-C₃N₄@ppy-rGO 3D structure hydrogel for efficient photocatalysis, *Appl. Surf. Sci.* 466 (2019) 666-672.
- [31] B. Tahir, M. Tahir, M.G.M. Nawawi, Highly stable honeycomb structured 2D/2D vanadium aluminum carbide MAX coupled g-C₃N₄ composite for stimulating photocatalytic CO₂ reduction

- to CO and CH₄ in a monolith photoreactor, *J. Alloy. Compd.* 927 (2022) 166908.
- [32] M. Tahir, Vanadium Carbide (V₂CTx) MXene-Supported Exfoliated g-C₃N₄ with the Role of Hole Scavenger as a Rapid Electron Transfer Channel for Enhancing Photocatalytic CO₂ Reduction to CO and CH₄, *Energy Fuels* 37 (2023) 10615-10630.
- [33] J. Li, Q. Zhang, Y. Zou, Y. Cao, W. Cui, F. Dong, Y. Zhou, Ti₃C₂ MXene modified g-C₃N₄ with enhanced visible-light photocatalytic performance for NO purification, *J. Colloid Interf. Sci.* 575 (2020) 443-451.
- [34] P. Lin, J. Shen, X. Yu, Q. Liu, D. Li, H. Tang, Construction of Ti₃C₂ MXene/O-doped g-C₃N₄ 2D-2D Schottky-junction for enhanced photocatalytic hydrogen evolution, *Ceram. Int.* 45 (2019) 24656-24663.
- [35] X. Zhang, Z. Zhang, Z. Zhou, MXene-based materials for electrochemical energy storage, *J. Energy Chem.* 27 (2018) 73-85.
- [36] X. Bao, H. Li, Z. Wang, F. Tong, M. Liu, Z. Zheng, P. Wang, H. Cheng, Y. Liu, Y. Dai, Y. Fan, Z. Li, B. Huang, TiO₂/Ti₃C₂ as an efficient photocatalyst for selective oxidation of benzyl alcohol to benzaldehyde, *Appl. Catal. B Environ.* 286 (2021) 119885.
- [37] B. He, Y. Du, Y.B. Feng, M.X. Du, J.Y. Wang, J.N. Qu, Y. Liu, N. Jiang, J.J. Wang, X.Y. Sun, Fabrication of novel ternary direct Z-scheme plus isotype heterojunction photocatalyst g-C₃N₄/g-C₃N₄/BiOBr with enhanced photocatalytic performance, *Appl. Surf. Sci.* 506 (2020) 10.
- [38] J. Gu, J. Yan, Z. Chen, H. Ji, Y. Song, Y. Fan, H. Xu, H. Li, Construction and preparation of novel 2D metal-free few-layer BN modified graphene-like g-C₃N₄ with enhanced photocatalytic performance, *Dalton T.* 46 (2017) 11250-11258.
- [39] F. Liu, T.-P. Nguyen, Q. Wang, F. Massuyeau, Y. Dan, L. Jiang, Construction of Z-scheme g-C₃N₄/Ag/P₃HT heterojunction for enhanced visible-light photocatalytic degradation of tetracycline (TC) and methyl orange (MO), *Appl. Surf. Sci.* 496 (2019) 143653.
- [40] Z. Lu, W. Song, M. Liu, Enhanced Visible-Light-Driven Photocatalytic Activity by Fe(capital SHA, Cyrillic)-Doped Graphitic C₃N₄, *Molecules* 27 (2022) 6986.
- [41] Y. Li, S. Li, C. Chao, S. Yao, D. Zhang, Q. Chen, Enhanced visible-light activation of persulfate by g-C₃N₄ decorated graphene aerogel for methyl orange degradation, *J. Alloy. Compd.* 926 (2022) 166904.
- [42] B. Zeng, X. Ning, L. Li, Fabrication and photocatalytic performance of highly active exposed facets ZnO hexagonal cap/Ti₃C₂ MXene composites, *J. Alloy. Compd.* 963 (2023) 171309.
- [43] X. Mu, L. Chen, N. Qu, J. Yu, X. Jiang, C. Xiao, X. Luo, Q. Hasi, MXene/polypyrrole coated melamine-foam for efficient interfacial evaporation and photodegradation, *J. Colloid Interf. Sci.* 636 (2023) 291-304.
- [44] Z. Guo, S. Ni, H. Wu, J. Wen, X. Li, T. Tang, M. Li, M. Liu, Designing nitrogen and phosphorus co-doped graphene quantum dots/g-C₃N₄ heterojunction composites to enhance visible and ultraviolet photocatalytic activity, *Appl. Surf. Sci.* 548 (2021) 149211.
- [45] Y. Wang, X. Wang, Y. Ji, R. Bian, J. Li, X. Zhang, J. Tian, Q. Yang, F. Shi, Ti₃C₂ MXene coupled with CdS nanoflowers as 2D/3D heterostructures for enhanced photocatalytic hydrogen production activity, *Int. J. Hydrogen Energ.* 47 (2022) 22045-22053.
- [46] Q. Lin, G. Zeng, S. Pu, G. Yan, J. Luo, Y. Wan, Z. Zhao, A dual regulation strategy for MXene-based composite membrane to achieve photocatalytic self-cleaning properties and multi-functional applications, *Chem. Eng. J.* 443 (2022) 136335.
- [47] Z. Wang, Z. Lin, S. Shen, W. Zhong, S. Cao, Advances in designing heterojunction photocatalytic

materials, Chinese J. Catal. 42 (2021) 710-730.